

# ERX: A Fast Real-Time Anomaly Detection Algorithm for Hyperspectral Line-Scanning

Samuel Garske , Bradley Evans , Christopher Artlett , and KC Wong 

**Abstract**—Detecting unexpected objects (anomalies) in real-time has great potential for monitoring, managing, and protecting the environment. Hyperspectral line-scan cameras are a low-cost solution that enhance confidence in anomaly detection over RGB and multispectral imagery. However, real-time algorithms for these cameras must be fast when using small computers (e.g., those onboard a drone or small satellite), scalable to high dimensions, adaptable to changing scenery, and robust against geometric and radiometric distortions. This paper introduces the Exponentially moving RX algorithm (ERX) and compares it to existing RX-based anomaly detection methods for real-time line-scanning. ERX was tested using a Jetson Xavier NX compute module, achieving the best combination of speed and detection across three novel datasets compared to the other algorithms. This research paves the way for future studies in grouping and locating anomalous objects, adaptive and automatic threshold selection, and real-time field tests. The Python code for the algorithms and experiments is available at <https://github.com/WiseGamgee/HyperAD>.

**Index Terms**—Anomaly Detection, Hyperspectral, Line-Scanning, Real-Time, Unsupervised Learning.

## I. INTRODUCTION

**A**NOMALY detection is an extremely useful task for finding unexpected objects in an image. It is an unsupervised learning task where no prior information or annotated examples of the anomalies are needed [1]. Detecting volcanic hotspots [2], identifying defects in manufactured products [3], and finding medical markers for the diagnosis of disease [4] are examples of image-based anomaly detection.

Detecting anomalies in real-time offers an advantage for applications that require fast and autonomous decision making. This has great potential in hyperspectral imaging for remote sensing; a rapidly growing area of research used to monitor, manage, and protect the environment [5]–[10]. Hyperspectral imaging, also known as imaging spectroscopy, provides greater confidence than RGB or multispectral imaging when detecting anomalies. This is because the pixels in a hyperspectral

This work was supported by the Australian Research Council through the Industrial Transformation Training Centre grant IC170100023 that funds the Australian Research Council (ARC) Training Centre for CubeSats, UAVs & Their Applications (CUAVA).

Samuel Garske and KC Wong are with the School of Aerospace, Mechanical, and Mechatronic Engineering, The University of Sydney, NSW 2006, Australia (e-mail: sam.garske@sydney.edu.au).

Bradley Evans is with the School of Environmental and Rural Science, The University of New England, Armidale, NSW 2350, Australia.

Christopher Artlett is with the Defence Science and Technology Group, Eveleigh, NSW 2015, Australia.

Samuel Garske, Bradley Evans, and KC Wong are also with CUAVA.

This work has been submitted to the IEEE for possible publication. Copyright may be transferred without notice, after which this version may no longer be accessible.

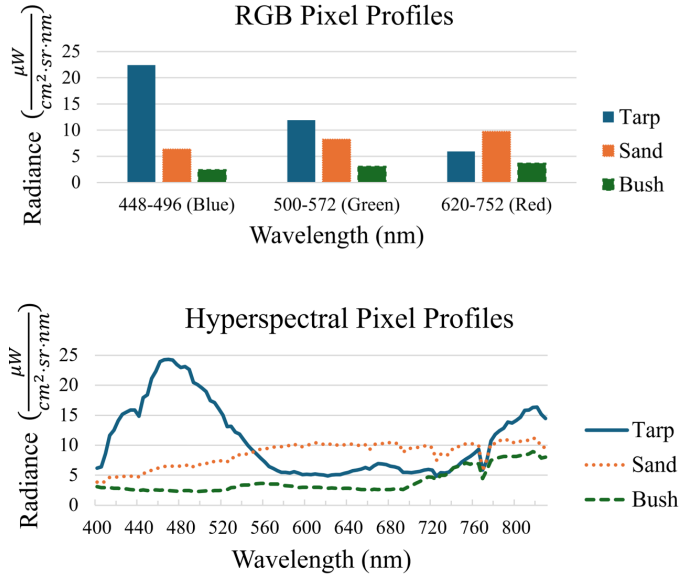
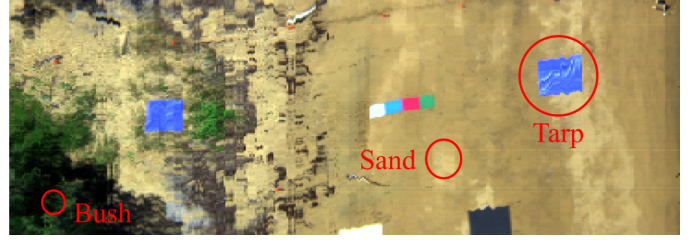


Fig. 1: Comparison of RGB vs HSI pixel profiles for various objects. The top image shows a section of the beach dataset from section IV-A, with pixels extracted from a tarp, sand, and bush (vegetation). Hyperspectral pixels (bottom) provide a detailed and continuous spectral profile via narrower bands, compared to the discrete RGB counterparts (middle). The RGB bands use the average radiance across the defined wavelength range.

image (HSI) have more detailed spectral profiles that uniquely represent the material present [11], as shown in Figure 1. The greater depth of spectral information can make it easier to separate anomalies from the background [1].

This study focuses specifically on anomaly detection using hyperspectral line-scan cameras, as they are an increasingly popular choice of camera for remote sensing applications. Real-time anomaly detection applications that use these cameras include search and rescue [12], defence surveillance and reconnaissance [13], and hazard detection in agricultural harvesting [14].

Hyperspectral line-scan cameras capture one line of pixels

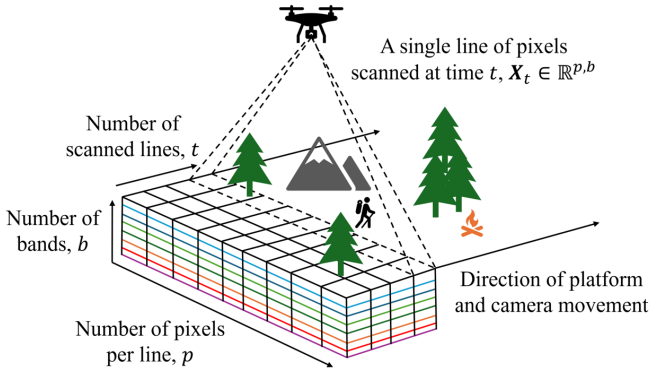


Fig. 2: A line-scan camera capturing one line of pixels at a time as it's platform (e.g., a drone) moves over the area of interest. These lines form a hyperspectral image, or datacube, with the depth dimension  $b$  representing the spectral bands for each pixel.

at a time and require the motion of an attached platform such as a drone, aircraft, or satellite to collect an image (Figure 2). They have relatively high signal-to-noise ratios [15], high spatial-spectral resolutions [16], and are easier and cheaper to build with commercially available components.

However, line-scan cameras are sensitive to unexpected platform movement and vibrations, causing distortions that require geometric correction when creating an image [16]. Each line also needs radiometric correction to convert the raw line-scan data into physically meaningful units, such as reflectance. Both processes are challenging and time-consuming, and are typically performed in post-processing. Therefore, it is proposed that real-time anomaly detection algorithms should have the following characteristics:

- Speed - fast processing for real-time results is essential to match the line-scan camera's image capture, so algorithm compute time should be minimised for field implementation (e.g., onboard drones or satellites).
- Scalability - leverages the numerous bands in HSIs.
- Adaptability - manages concept drift and non-stationary behaviour, referring to changing distribution of imagery over time, crucial for monitoring large areas with varying scenery and lighting.
- Robustness - maintains strong performance when operating with geospatial distortions present and less radiometric correction (e.g., using radiance instead of reflectance).

The benchmark method for the detection of hyperspectral anomalies is the Reed-Xiaoli (RX) algorithm [17]. Given a hyperspectral image, the mean pixel vector (1) and the covariance matrix (2) are calculated using every pixel:

$$\boldsymbol{\mu} = \frac{1}{n} \sum_{i=1}^n \mathbf{x}_i \quad (1)$$

$$\mathbf{K} = \frac{1}{n} \sum_{i=1}^n (\mathbf{x}_i - \boldsymbol{\mu})(\mathbf{x}_i - \boldsymbol{\mu})^T \quad (2)$$

where  $\mathbf{x}_i \in \mathbb{R}^b$  represents each pixel,  $b$  is the number of hyperspectral bands, and  $n$  is the total number of pixels in the image. The mean and covariance model the image background

using a normal distribution. The Mahalanobis distance (3) is then calculated for each pixel:

$$\delta_i = \sqrt{(\mathbf{x}_i - \boldsymbol{\mu})\mathbf{K}^{-1}(\mathbf{x}_i - \boldsymbol{\mu})^T} \quad (3)$$

The Mahalanobis distance gives an estimate of how far each pixel lies from the background, where a larger distance means a greater likelihood of being an anomaly. Finally, pixels are classified as anomalous if their distance is above a user-defined threshold ( $T$ ):

$$\hat{y}_i = \begin{cases} 1, & \text{if } \delta_i \geq T \\ 0, & \text{otherwise} \end{cases} \quad (4)$$

Although the RX algorithm is effective for identifying anomalies in HSIs, it is not designed for real-time implementation. Real-time implementation requires a sequential, time-series approach that only accesses past and present data. Many more methods have been established since the RX algorithm for detecting anomalies in HSIs, ranging from simpler traditional statistics and distance-based metrics to more complex unsupervised deep learning models [18]. However, only a small fraction of these anomaly detection algorithms are suitable for processing line-scan imagery in real-time. As such, the aims of this research are:

- 1) To provide a review of real-time RX-based hyperspectral line-scan anomaly detection algorithms.
- 2) To present the Exponentially moving RX anomaly detector (ERX); an algorithm that is fast, scalable, adaptable, and robust.
- 3) To evaluate ERX on a small edge computer and benchmark it's performance against similar algorithms using various high-dimensional datasets.

## II. RELATED WORK

This section summarises RX-based algorithms that are used for real-time line-scan anomaly detection. The algorithms are separated into subsections that share common methods. A limitation of the RX algorithm is that it requires capturing every single pixel before calculating the mean and covariance of a HSI. This prevents detecting hyperspectral anomalies in real-time and easily results in insufficient memory due to the large amount of data in HSIs. Furthermore, calculating the inverse of the covariance matrix is a slow operation in the RX algorithm because of the large number of hyperspectral bands. A common solution to these issues is to perform recursive mean and covariance updates, of which one popular method is the Woodbury Matrix Identity.

### A. The Woodbury Matrix Identity

The Woodbury matrix identity (5) is an expression that has been used to recursively update the inverse covariance matrix as new lines are captured from the camera, reducing both memory requirements and compute time.

$$[\mathbf{A} + \mathbf{u}\mathbf{c}\mathbf{v}^T]^{-1} = \mathbf{A}^{-1} - \frac{[\mathbf{A}^{-1}\mathbf{u}][\mathbf{v}\mathbf{A}^{-1}]}{\mathbf{c}^{-1} + \mathbf{v}\mathbf{A}^{-1}\mathbf{u}} \quad (5)$$

Chen et al. [19] presented the real-time causal RXD algorithm, RT-CK-RXD. RT-CK-RXD detects anomalies pixel-wise, which means that it iterates over each pixel in a new line. Chen et al. redefined the current covariance estimate  $\mathbf{K}_t$  (2) as a function of its previous value  $\mathbf{K}_{t-1}$  and the current pixel  $\mathbf{x}_t$ , shown in equation (6):

$$\mathbf{K}_t = \frac{n-1}{n}\mathbf{K}_{t-1} + \frac{1}{n}(\mathbf{x}_t - \boldsymbol{\mu}_t)(\mathbf{x}_t - \boldsymbol{\mu}_t)^T \quad (6)$$

where  $n$  is the total number of pixels processed at time  $t$ . By inverting (6), the inverse covariance was then equated to the LHS of the Woodbury Matrix identity equation in (5), giving:

$$\mathbf{K}_t^{-1} = \left[ \frac{n-1}{n}\mathbf{K}_{t-1} + \frac{1}{n}(\mathbf{x}_t - \boldsymbol{\mu}_t)(\mathbf{x}_t - \boldsymbol{\mu}_t)^T \right]^{-1} \quad (7)$$

Identifying  $\mathbf{A} = \frac{n-1}{n}\mathbf{K}_{t-1}$ ,  $\mathbf{u} = \mathbf{v} = \frac{1}{\sqrt{n}}(\mathbf{x}_t - \boldsymbol{\mu}_t)$ , and  $c = 1$ , these values are substituted into the RHS of (5) and the inverse covariance matrix is updated.

Chen et al. [19] also define RT-CR-RXD, which replaces the covariance matrix with the correlation matrix  $\mathbf{R}_t = \frac{1}{n} \sum_{i=1}^n \mathbf{x}_i \mathbf{x}_i^T$ . This algorithm is a faster alternative, as the correlation matrix does not require demeaning of each pixel while still extracting the correlation between the hyperspectral bands.

Du and Nekovei [20] proposed several in-depth RX algorithms for real-time anomaly detection. One algorithm, RX-BIL, used the generalised Woodbury matrix identity to update the inverse correlation matrix for each new line  $\mathbf{X}_t$ :

$$\mathbf{R}_t^{-1} = \mathbf{R}_{t-1}^{-1} - \frac{[\mathbf{R}_{t-1}^{-1} \mathbf{X}_t][\mathbf{X}_t^T \mathbf{R}_{t-1}^{-1}]}{\mathbf{I} + \mathbf{X}_t^T \mathbf{R}_{t-1}^{-1} \mathbf{X}_t} \quad (8)$$

Furthermore, RX-BIL randomly removed pixels to increase detection speed. More pixels can be removed in homogeneous images as fewer are needed to accurately estimate the background mean and covariance. Fewer pixels should be removed in diverse images, so that more variable spectra are captured by the background statistics.

Liu et al. [21] combined the Woodbury matrix identity with a finite Markov model for a line-wise anomaly detection algorithm, FMLRT-RAD. The addition of the finite Markov model improved the detection stability and adaptability by removing “redundant” information from previous lines. Compared to RT-CR-RXD, Liu et al. found that FMLRT-RAD had slightly higher detection performance and slightly slower, but comparable, processing speed.

### B. Cholesky Decomposition

While the Woodbury matrix identity offers a fast way to update the inverse covariance, Cholesky decomposition paired with forward substitution avoids calculating the inverse covariance altogether. Zhang et al. [22] proposed CDLSS, a line-wise anomaly detection algorithm that used Cholesky decomposition. Given a new line of pixels  $\mathbf{X}_t$ , the corresponding Mahalanobis distance of each pixel defined as:

$$\delta_i = \sqrt{\mathbf{x}_i \mathbf{R}_{t-1}^{-1} \mathbf{x}_i^T} \quad (9)$$

where  $\mathbf{x}_i$  is the  $i$ th pixel vector in line  $\mathbf{X}_t$ , and  $\mathbf{R}_{t-1}$  is the correlation matrix in the previous time step. The correlation

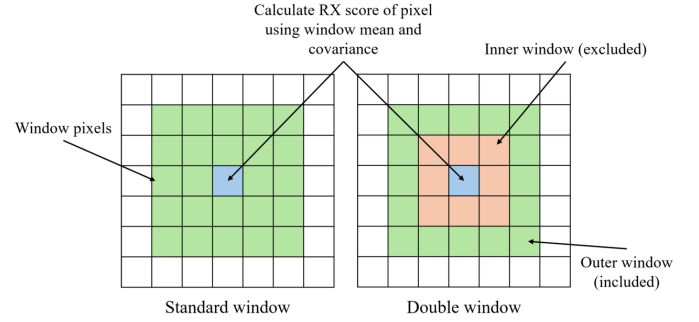


Fig. 3: A standard window (left) versus a double window (right). The central pixel (blue) is analysed, with each approach estimating the local mean and covariance from the surrounding pixels.

matrix is decomposed into its lower triangle matrix representation  $\mathbf{R}_{t-1} = \mathbf{L}_{t-1} \mathbf{L}_{t-1}^T$ , which can be substituted into (9):

$$\delta_i = \sqrt{(\mathbf{x}_t \mathbf{L}_{t-1}^{-1})(\mathbf{x}_t \mathbf{L}_{t-1}^{-1})^T} \quad (10)$$

By substituting in  $(\mathbf{X}_t \mathbf{L}_{t-1}^{-1}) = \mathbf{z}_i$ , the Mahalanobis distance is represented as:

$$\delta_i = \sqrt{\mathbf{z}_i \cdot \mathbf{z}_i} \quad (11)$$

As  $\mathbf{x}_i$  is known and  $\mathbf{L}_{t-1}$  is calculated from Cholesky decomposition, forward substitution is used to calculate  $\mathbf{z}_i$  directly, given that  $\mathbf{z}_i \mathbf{L}_{t-1} = \mathbf{x}_i$ .

Zhao and Xi-Feng [23] presented LRT-KRXD-CD, using Cholesky decomposition to reduce the processing time of the local real-time kernel RX detector (LRT-KRXD) [24]. Zhao et al. [25] presented RT-KCRD, building on KCRD [26] with Cholesky decomposition method. RT-KCRD used a moving window (discussed in the following section), recursive updates for the kernel covariance matrix, and an optimised regularisation matrix using previous anomaly scores. RT-KCRD was on average 86 times faster than KRXD and KCRD, and was comparable to LRT-KRXD-CD [25].

### C. Local/Window Algorithms

Window-based algorithms extract anomalies locally rather than at a global level, improving detection performance [27]. As shown in Figure 3, a standard window is a small region surrounding the current pixel being processed. Double-windows discard a small inner region of pixels, minimising the contribution of the same object to the local background statistics.

Rossi et al. [28] improved two local anomaly detection algorithms using fast updates of the inverse covariance. The first, RX-LBL-IU, builds off the work of Acito et al. [29], which used “sliding” double-windows around each pixel to identify anomalies. The sliding window approach used the Woodbury matrix identity to recursively update the window inverse covariance, instead of recalculating it for each pixel’s window. The second method is Dark HORSE RX [13], which used an exponentially rolling mean and covariance for pixel-wise updates. Rossi et al. [28] deemed RX-LBL-IU the most effective of the two algorithms.

Zhao et al. [30] presented a causal pixel-wise approach, only accessing the window pixels captured before the current pixel being analysed. A two-step Woodbury matrix identity was used to update the inverse correlation matrix by adding the latest pixel and removing the oldest one.

Although window methods provide localised anomaly detection, a major challenge is calculating the window statistics efficiently. Small window sizes commonly led to matrix singularities, and large window sizes led to slow compute times. Preliminary experiments showed that they were too slow for real-time detection on the Jetson using Python.

#### D. Kernel Methods

Kernel methods addressed the assumption of a normal distribution in the RX algorithm and subsequently improved detection accuracy. A kernel function allows the RX algorithm to map the non-linear correlations that hyperspectral bands share between one another in practice [31]. PLP-KRXD was proposed by Zhao et al. [32], using parallel sliding windows and the Woodbury matrix identity to speed up the KRX algorithm [31]. The sliding windows were implemented as a faster alternative to the double-window model. The Woodbury matrix identity reduced the time required to calculate the inverse covariance of multiple sliding windows. Zhao et al. demonstrated that PLP-KRXD achieved similar detection performance to KRXD, but was 40 to 58 times faster depending on the dataset. Kernel methods, despite their higher anomaly detection accuracy, are slower due to additional matrix operations.

#### E. Dimensionality Reduction

Dimensionality reduction methods improve processing speed and signal-to-noise ratio by transforming hyperspectral bands into fewer features. Horstrand et al. [14] developed LbL-AD, which uses Principal Component Analysis (PCA) to reduce the number of bands. A line-wise subspace calculation using the power method and deflation was used to efficiently approximate the eigenvalues  $e_t$  and the eigenvectors  $E_t$ . Using orthogonal subspace projection, the dimensions of the hyperspectral line were reduced:

$$\mathbf{Z}_t = \mathbf{E}_t^T \mathbf{X}_t \quad (12)$$

where  $\mathbf{X}_t$  is the most recent hyperspectral line and  $\mathbf{S}_t$  is the line after the dimensionality reduction, with the eigenvalues  $e_t$  forming the diagonal of the lower-dimensional covariance matrix. The Mahalanobis distance was calculated as:

$$\delta_i = \sqrt{\mathbf{s}_i \text{diag}(\mathbf{e}_t)^{-1} \mathbf{s}_i^T} \quad (13)$$

where  $\mathbf{s}_i$  is the  $i$ th dimensionality-reduced pixel in the current line. The authors introduced an adaptive threshold method to detect anomalous pixels by excluding their contribution to background statistics.

LbL-FAD was also proposed, using a modified Gram-Schmidt method for orthogonal subspace projection [33]. This algorithm has also been adapted for hardware through field-programmable gate arrays (FPGAs), demonstrating the efficiency of the algorithm onboard small platforms in real-time [34], [35].

### III. PROPOSED ALGORITHM - ERX

The Exponentially moving RX detector (ERX) uses exponentially moving averages to perform rapid updates to the background mean and covariance while keeping memory requirements low. The use of exponential weightings allows for a combination of global and local anomaly detection.

For a new hyperspectral line collected  $\mathbf{X}_t \in \mathbb{R}^{p,b}$ , the mean vector and covariance matrix are estimated:

$$\bar{\mathbf{x}}_t = \frac{1}{p} \sum_{i=1}^p \mathbf{x}_i \quad (14)$$

$$\bar{\mathbf{K}}_t = \frac{1}{p-1} \sum_{i=1}^p (\mathbf{x}_i - \bar{\mathbf{x}}_t)(\mathbf{x}_i - \bar{\mathbf{x}}_t)^T \quad (15)$$

where each pixel in  $\mathbf{X}_t$  is defined as  $\mathbf{x}_i \in \mathbb{R}^b$  ( $b$  is the number of bands,  $p$  is the number of pixels per line, and  $i = 1, 2, \dots, p$ ). The background mean and covariance are then updated using a momentum factor  $\alpha$  (where  $0 < \alpha < 1$ ):

$$\boldsymbol{\mu}_t = (1 - \alpha)\boldsymbol{\mu}_{t-1} + \alpha\bar{\mathbf{x}}_t \quad (16)$$

$$\mathbf{K}_t = (1 - \alpha)\mathbf{K}_{t-1} + \alpha\bar{\mathbf{K}}_t \quad (17)$$

Increasing  $\alpha$  weighs recent lines more heavily, and decreasing  $\alpha$  puts more weight on the initial background statistics. With the background statistics calculated, the Mahalanobis distance each pixel is defined as:

$$\delta_i = \sqrt{(\mathbf{x}'_i - \boldsymbol{\mu}_t)\mathbf{K}_t^{-1}(\mathbf{x}'_i - \boldsymbol{\mu}_t)^T} \quad (18)$$

where  $\mathbf{x}'_i$  is each pixel in the previously captured line  $\mathbf{X}_{t-o}$ ,  $o$  being a small offset. Calculating the Mahalanobis distance of a previous line allows ERX to incorporate spatial information ahead of the pixel when estimating the background mean and covariance. Like Zhang et al. [22], Cholesky decomposition is used on the covariance matrix, giving:

$$\delta_i = \sqrt{[(\mathbf{x}'_i - \boldsymbol{\mu}_t)\mathbf{L}_t^{-1}][(\mathbf{x}'_i - \boldsymbol{\mu}_t)\mathbf{L}_t^{-1}]^T} \quad (19)$$

where  $\mathbf{L}_t$  is the lower triangle of  $\mathbf{K}_t^{-1} + 10^{-5}\mathbf{I}$ . The small identity matrix  $10^{-5}\mathbf{I}$  is added to the covariance matrix prior to Cholesky decomposition to prevent matrix singularities and improve the stability of the algorithm. (19) can be simplified by substituting  $\mathbf{z}_i = (\mathbf{x}'_i - \boldsymbol{\mu}_t)\mathbf{L}_t^{-1}$ :

$$\delta_i = \sqrt{\mathbf{z}_i \cdot \mathbf{z}_i^T} \quad (20)$$

where  $\mathbf{z}_i$  is calculated directly using forward substitution for  $\mathbf{L}_t \mathbf{z}_i = (\mathbf{x}'_i - \boldsymbol{\mu}_t)$ , avoiding the inversion of the covariance matrix. The Mahalanobis distance vector is then normalised across the line:

$$\delta_{N,i} = \frac{\delta_i - \bar{\delta}}{\sigma_\delta} \quad (21)$$

where  $\bar{\delta}$  is the mean Mahalanobis distance and  $\sigma_\delta$  is the standard deviation. Pixels in the line are defined as an anomaly if they are above a threshold value  $T_N$ :

$$\hat{y}_i = \begin{cases} 1, & \text{if } \delta_{N,i} \geq T_N \\ 0, & \text{otherwise} \end{cases} \quad (22)$$

An optimised pseudo-code version of the algorithm is detailed in algorithm 1, with vector notation and broadcasting assumed to speed up processing.

---

**Algorithm 1** ERX Algorithm
 

---

**Input:**  $\mathbf{X}_t$ : current line matrix,  $\boldsymbol{\mu}_{t-1}$ : previous mean vector,  $\mathbf{K}_{t-1}$ : previous covariance matrix, **buffer**: rolling buffer with  $l$  previous lines,  $\alpha$ : momentum value,  $o$ : line offset,  $n_l$ : the total number of lines processed so far,  $T_N$ : normalised threshold value.

**Output:**  $\mathbf{y}_t$ : binary vector of anomaly detections in line,  $\boldsymbol{\mu}_t$ : new mean vector,  $\mathbf{K}_t$ : new covariance matrix, **buffer**: updated buffer.

```

1: procedure PROCESSLINE( $\mathbf{X}_t, \boldsymbol{\mu}_{t-1}, \mathbf{K}_{t-1}, \mathbf{buffer}, \alpha, o,$ 
    $n_l, T_N$ )
2:    $\bar{\mathbf{x}}_t \leftarrow \text{mean}(\mathbf{X}_t)$ 
3:    $\bar{\mathbf{K}}_t \leftarrow \text{covariance}(\mathbf{X}_t)$ 
4:   buffer  $\leftarrow$  buffer.append( $\mathbf{X}_t$ )
5:   buffer  $\leftarrow$  buffer.remove( $\mathbf{X}_{t-l}$ )
6:   if  $n_l = 0$  then
7:      $\boldsymbol{\mu}_t \leftarrow \bar{\mathbf{x}}_t$ 
8:      $\mathbf{K}_t \leftarrow \bar{\mathbf{K}}_t$ 
9:   else
10:     $\boldsymbol{\mu}_t \leftarrow \boldsymbol{\mu}_{t-1} - \alpha(\boldsymbol{\mu}_{t-1} - \bar{\mathbf{x}}_t)$ 
11:     $\mathbf{K}_t \leftarrow \mathbf{K}_{t-1} - \alpha(\mathbf{K}_{t-1} - \bar{\mathbf{K}}_t)$ 
12:   if  $n_l \geq l$  then
13:      $\mathbf{X}_{t-o} \leftarrow \mathbf{buffer}[t-o]$ 
14:      $\mathbf{L}_t \leftarrow \text{cholesky}(\mathbf{K}_t + 10^{-5}\mathbf{I}_b)$ 
15:      $\boldsymbol{\Delta}_t \leftarrow \mathbf{X}_{t-o} - \boldsymbol{\mu}_t$ 
16:      $\mathbf{z}_t \leftarrow \text{solve}(\mathbf{L}_t, \boldsymbol{\Delta}_t^T)$ 
17:      $\boldsymbol{\delta}_t \leftarrow \text{norm}(\mathbf{z}_t)$ 
18:      $\boldsymbol{\delta}_N \leftarrow \frac{\boldsymbol{\delta}_t - \text{mean}(\boldsymbol{\delta}_t)}{\text{variance}(\boldsymbol{\delta}_t)}$ 
19:      $\hat{\mathbf{y}}_t \leftarrow \text{array}(\text{len}(\boldsymbol{\delta}_N))$ 
20:     for  $i = 1$  to  $\text{len}(\hat{\mathbf{y}}_t)$  do
21:       if  $\boldsymbol{\delta}_N[i] \geq T_N$  then
22:          $\hat{\mathbf{y}}_t[i] \leftarrow 1$ 
23:       else
24:          $\hat{\mathbf{y}}_t[i] \leftarrow 0$ 
25:    $n_l \leftarrow n_l + 1$ 
26:   return  $\mathbf{y}_t, \boldsymbol{\mu}_t, \mathbf{K}_t, \mathbf{buffer}, n_l$ 

```

---

#### IV. EXPERIMENTS & RESULTS

This section includes the datasets, experimental designs, and the results. The Python code for all algorithms and their experiments is available at <https://github.com/WiseGamagee/HyperAD>.

##### A. Datasets

Three datasets are used to evaluate the performance of each algorithm, being fed line-by-line to simulate the capture of a line-scan camera (from left to right for each image):

- Beach dataset - a natural coastal area with a variety of human-made anomalies present (Figure 4).
- Synthetic dataset - a constructed dataset using pixels sampled from AVIRIS with anomalous targets (Figure 5).
- Sequoia National Park (SNP) dataset - a national park with live wildfires present (Figure 6).

The beach dataset, sized 452 pixels by 3072 lines with 108 bands, was collected via a drone-mounted hyperspectral line-scan system on a beach in Queensland, Australia. It transitions

from vegetation, to sand, to shallow ocean, and includes anomalous objects such as different coloured and sized tarps, two vehicles, and reflective cones (the smaller yellow objects in the ground truth). This version uses radiance and lacks geometric correction, as is evident from the "wobble" between lines in Figure 4. For more details, see Mao et al. [36].

The synthetic dataset, sized 600 pixels by 2400 lines with 90 bands, was created by sampling pixels from an AVIRIS radiance dataset collected near Gulfport, Mississippi [37]. The background is generated from vegetation, sand, and water pixels with smoothed transitions between each type. The anomalies are square targets made from airport runway pixels. The targets are equally spaced with decreasing size along-track (left to right), and are repeated from top to bottom with 0%, 10%, 20%, 30%, and 50% background mixing to add noise. The original 224 bands are reduced to 189 by removing the water absorption and low signal-to-noise ratio bands (as in Głomb and Romaszewski [38]). After this, only the first 90 bands are kept to further improve the signal-to-noise ratio and avoid the OpenBLAS threading issue (discussed in Section V-A).

The Sequoia National Park (SNP) dataset, 1116 pixels by 2499 lines with 13 bands, was collected using the Sentinel 2 multispectral satellites. The dataset is of a section of the Sequoia National Park in California, U.S.A and includes live wildfires as anomalies which were identified using the infrared bands. It uses level-1c processing for top-of-atmosphere reflectance, unlike the hyperspectral datasets that use radiance. This multispectral dataset helps demonstrate algorithm performance on lower dimensional data.

##### B. Anomaly Detection Algorithms

The following algorithms are tested on the datasets:

- 1) RX Baseline.
- 2) RT-CK-RXD [19].
- 3) RX-BIL [20].
- 4) LBL-AD [14].
- 5) ERX, presented in algorithm 1.

TABLE I: Normalised Mahalanobis Distance Threshold Values ( $T_N$ ) for Every Algorithm and Dataset.

Algorithm	Beach Dataset	Synthetic Dataset	SNP Dataset
RX Baseline	1.5	3	5
RT-CK-RXD	1.5	3	5
RX-BIL	1.5	3	5
LBL-AD	1.5	1.5	4
ERX	1.5	3	5

The RX Baseline algorithm serves as a benchmark for real-time line-scan anomaly detection. A rolling buffer stores the last 99 lines. The mean vector and covariance matrix are calculated using the whole buffer, and the RX algorithm is applied to the centre line. This process is repeated for each new line (visualised in Figure 7).

RT-CK-RXD uses a buffer of length 99 for the initial mean and covariance estimates. This algorithm updates the mean and covariance and computes the Mahalanobis distance pixel-wise.

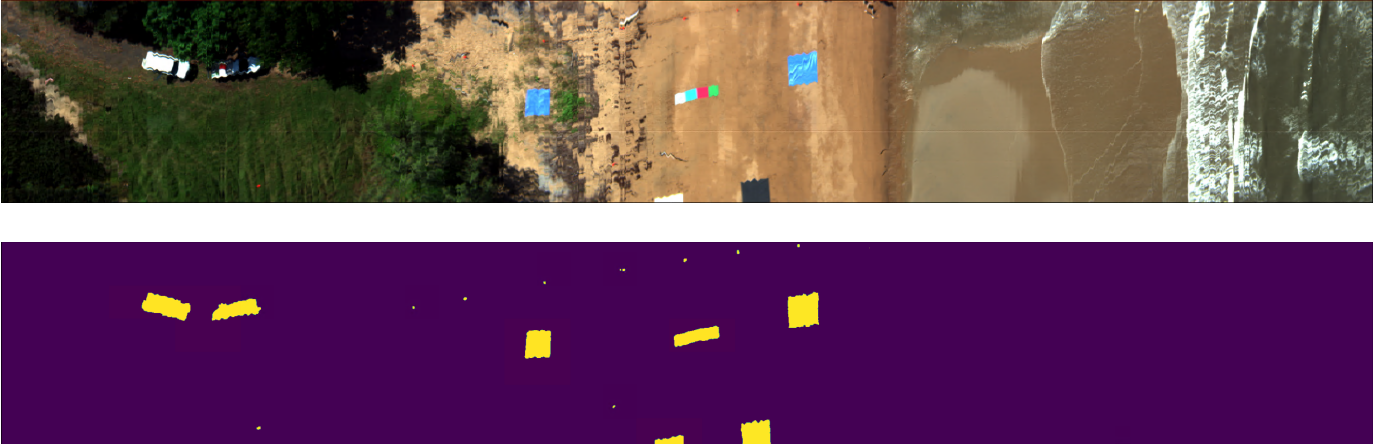


Fig. 4: The beach dataset RGB image (top) and anomaly ground truth image (bottom).

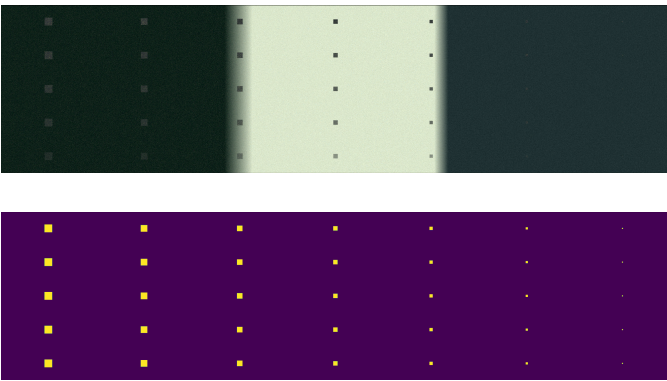


Fig. 5: The synthetic dataset RGB image (top) and anomaly ground truth image (bottom).

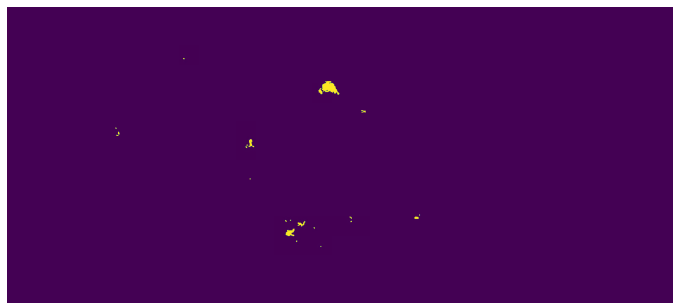


Fig. 6: The Sequoia National Park (SNP) dataset RGB image (top) and anomaly ground truth image (bottom). The dataset has few anomalous pixels, making it highly imbalanced.

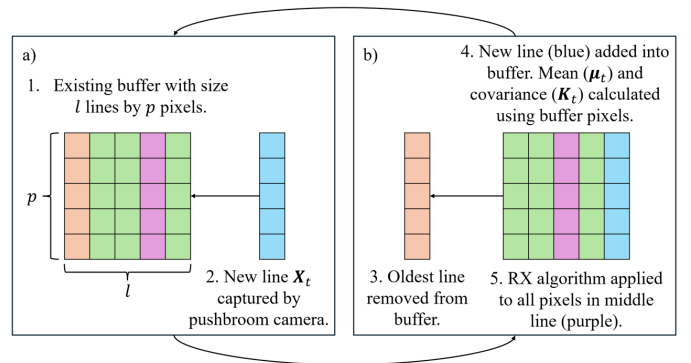


Fig. 7: Visualisation of the RX Baseline algorithm. This process is repeated for each new line captured by a line-scan camera in real-time.

Just-in-time compilation via Numba [39] is used to speed up inverse covariance updates.

RX-BIL also uses a 99 line buffer and randomly discards 50% of the pixels per line. Instead of initialising the mean vector and correlation matrices with small random numbers, the mean and correlation of the first line are used for initialisation, substantially speeding up convergence.

For LBL-AD, the bands are reduced to 3 principal components. Horstrand et al. [14] recommend a maximum of five principal components to avoid impacting speed too much. The automatic threshold component is not included, and Numba is used to speed up the power iteration algorithm.

ERX uses a buffer of length 99, an offset of  $o = 30$ , and a momentum factor of  $\alpha = 0.5$ . In practice, each algorithm needs a threshold selected to detect anomalous pixels. Optimal normalised thresholds (22) for each algorithm and dataset are determined by grid search and shown in Table I. The preset thresholds are used to demonstrate potential anomaly detection performance, but are noted as limiting due to needing prior information.

### C. Experiments

The first experiment evaluates the impact of varying the ERX momentum parameter  $\alpha$ . Two further experiments compare ERX's speed and detection performance to the other

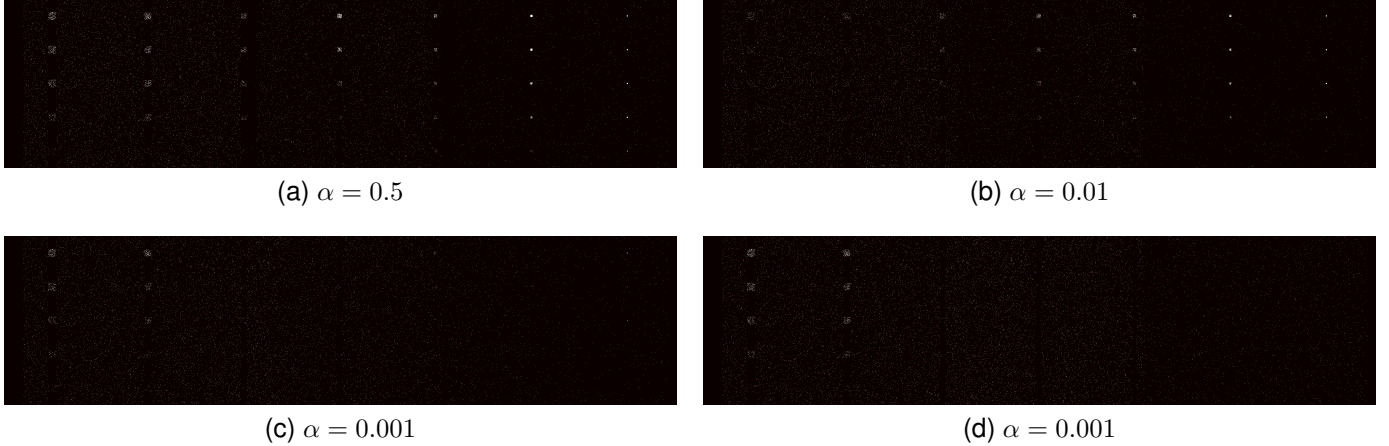


Fig. 8: ERX’s binary anomaly detection maps for various momentum values when applied to the synthetic dataset.

TABLE II: ERX Detection Results - Varying Momentum ( $\alpha$ ).

$\alpha$	Beach Dataset		Synthetic Dataset		SNP Dataset	
	F1	AUC	F1	AUC	F1	AUC
0.9	<b>0.463</b>	<b>0.848</b>	<b>0.157</b>	<b>0.855</b>	0.313	0.986
0.5	0.441	0.845	0.150	0.852	0.306	0.986
0.1	0.310	0.809	0.085	0.633	0.279	0.987
0.01	0.302	0.793	0.085	0.547	0.303	0.989
1e-3	0.369	0.801	0.060	0.503	0.397	0.992
1e-4	0.439	0.796	0.063	0.523	<b>0.483</b>	<b>0.993</b>
1e-5	0.450	0.789	0.070	0.530	0.444	0.993

algorithms. All experiments were carried out on an NVIDIA Jetson Xavier NX compute module with 8GB RAM, a 6-core NVIDIA Carmel ARMv8.2 CPU, and a 384-core NVIDIA Volta GPU with 48 Tensor cores, using the default 10W power mode.

1) *ERX Momentum Evaluation*: This experiment investigates the ERX momentum parameter  $\alpha$ , which modifies the algorithm’s detection performance based on anomaly size. The Area Under the ROC Curve (AUC) is used to assess performance across a range of thresholds  $T_N$ , and the F1 score is used because it is more robust than the AUC for highly imbalanced datasets. The thresholds used to calculate the F1 scores are defined in Table I. The results for each dataset are given in Table II. Additionally, binary anomaly maps of the synthetic dataset in Figure 8 demonstrate how momentum affects ERX’s detection performance.

2) *Speed Comparison*: This experiment compares the processing speed and scalability of the detection algorithms across increasing bands. Each algorithm is tested on the same randomly generated dataset of 500 pixels, 3,000 lines and 10 to 200 bands. The metric is the number of lines processed per second, averaged over 5 iterations. The results are shown in Figure 9.

3) *Detection Comparison*: This experiment compares the anomaly detection performance of each algorithm. Each algorithm is tested on each of the three datasets. The AUC and F1 score are used again to evaluate detection performance. The average processing speed is recorded across 5 iterations. The results are shown in Table III.

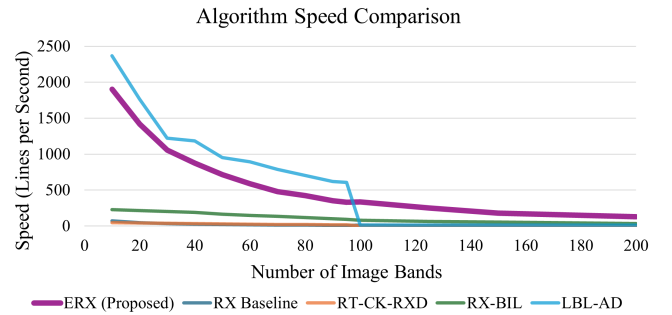


Fig. 9: A comparison all of the algorithms’ speed on the Jetson device with an increasing number of bands.

## V. DISCUSSION

### A. Results Discussion

Varying the momentum of ERX demonstrates that it can be tuned to improve detection performance in different scenarios (Table II). On the beach dataset, ERX performs the best for both very low momentum values (close to 0, which maintains the initial mean and covariance estimates from the first 99 lines which have no anomalies) and relatively high ones (closer to 1 which mostly uses the mean and covariance of the most recent line). Using momentum values between 1e-4 and 0.1 gives poorer detection performance for this dataset, because ERX is weighing anomalous pixels too heavily. Given that the beach dataset has a higher proportion of anomalous pixels, the heavier weighting leads to poorer background mean and covariance estimates.

The binary detection masks in Figure 8 indicate that smaller momentum values hinder ERX’s detection of the smaller targets at the end of the synthetic dataset, suggesting insufficient adaptation to the changing background. ERX performs best on the synthetic dataset for high momentum values, confirming that faster updates are advantageous when the scene distribution changes. This aligns with the results of the more homogeneous SNP dataset, where the best performance is for small momentum values. The consistently high AUC of the SNP dataset is expected from the high class imbalance.

TABLE III: Algorithm Detection Results for All Datasets (lps = lines per second).

Algorithm	Beach Dataset			Synthetic Dataset			SNP Dataset		
	F1 score	AUC	Speed (lps)	F1 score	AUC	Speed (lps)	F1 score	AUC	Speed (lps)
RX Baseline	0.275	0.778	15	0.074	0.531	8	0.282	0.988	48
RT-CK-RXD	0.419	0.805	<1	0.067	0.581	14	0.391	<b>0.992</b>	19
RX-BIL	0.419	0.803	73	0.070	0.566	64	0.377	<b>0.992</b>	32
LBL-AD	0.192	0.697	14	0.047	0.585	<b>386</b>	<b>0.576</b>	0.971	658
ERX	<b>0.441</b>	<b>0.845</b>	<b>273</b>	<b>0.150</b>	<b>0.852</b>	248	0.306	0.986	<b>886</b>

However,  $\alpha = 0.01$  causes ERX to miss larger targets (larger targets contribute too much to the background), while  $\alpha = 0.001$  and lower miss smaller targets (the exponential decay of previous targets is too slow). Thus, momentum optimisation also depends on the frequency and size of anomalies, and not just on the variability of the scenery.

The speed comparison (Figure 9) shows that ERX and LBL-AD are consistently faster than RX-Baseline, RX-BIL and RT-CK-RXD. Although LBL-AD is initially the fastest, ERX maintains the best performance as the number of bands moves past 100. The sharp drop in LBL-AD’s performance was found to occur upstream of Python, where the OpenBLAS library [40] for linear algebra computations switches from single-threading to multi-threading after a dimension size of 95 (i.e., greater than 95 bands). This issue arises when calling the Numpy dot product, which ERX avoids to maintain faster speeds at higher dimensions compared to the other algorithms.

Putting the results in the context of real-time operations, a modified OpenHSI camera that collected the beach dataset (108 band) operated at 120 lines per second with the Jetson. ERX, processing at 273 lines per second, is the only algorithm fast enough for real-time anomaly detection on the Jetson. It is also the fastest algorithm for the Sequoia National Park dataset.

The comparison in Table III shows that ERX outperforms in all metrics in the beach data set. RX-BIL and RT-CK-RXD detect comparatively well but are too slow for real-time processing. RT-CK-RXD failed to complete on the Jetson due to its pixel-wise approach and the OpenBLAS threading constraint. ERX is over three times faster than the next best algorithm, RX-BIL, on the Jetson.

ERX achieves the best detection scores and is the second fastest for the synthetic dataset. However, the performance of all algorithms is poor. The low F1 scores indicate many false detections and missed anomalies, and AUC scores near 0.5 mean that most algorithms are only slightly better than a random guessing. This shows that the synthetic data set is challenging. The high fraction of anomalous pixels compared to the beach and SNP datasets complicates separation from the background. The detection maps in figure 8 show that despite the low F1 score of ERX, it successfully identifies the structure of most targets. Therefore, object-based detection methods and metrics may be more practical than pixel-based approaches.

ERX has the fastest speed for the Sequoia National Park dataset but underperforms in detection. Reducing the momentum to  $1e - 4$  improves the F1 score, indicating 0.5 updates ERX too quickly. Given the results of the speed test (Figure 9), one would expect LBL-AD to be faster than ERX at

only 13 bands. This is a result of LBL-AD having a larger computational overhead on intialisation. However, LBL-AD excels in anomaly detection for this dataset, suggesting that it’s PCA approach works well with fewer bands. Further work is needed to confirm this hypothesis, and integrating similar dimensionality reduction techniques into ERX might enhance results.

### B. Limitations & Future Work

Creating an open-source Python repository improves accessibility and reproducibility for future projects, but at the cost of slower processing speeds. Implementing these algorithms in faster languages like C++ would significantly improve their processing speeds. If faster languages were used, more algorithm types, such as those using kernel and window methods, may become feasible for real-time applications. Performing field tests of these algorithms for extended periods, beyond simulations, is crucial for validating the results, adaptability, and practicality of the ERX algorithm.

This work lays a foundation for real-time RX-based pixel anomaly detection, although the generally low F1 and AUC scores highlighted an ongoing challenge in detecting anomalies at the pixel level. Grouping pixels into anomalous objects and locating them is a more useful task in practice and may yield better results with object-based metrics. Future research could explore unsupervised, self-supervised, and synthetically trained object detection algorithms (e.g., YOLO [41]). Rather than line-wise detection, using batches of hyperspectral lines could be more practical for detecting and locating anomalous objects in real-time, or at least near real-time.

Lastly, selecting optimal thresholds is a key challenge and requires further study for these methods to be fully unsupervised and out-of-the-box anomaly detection algorithms. Without prior knowledge, it is difficult to justify an effective Mahalanobis distance threshold value without data “snooping” into test datasets. Adaptive threshold selection has been briefly explored [14], [42], leaving room for future contributions. Less supervised models, such as those using few-shot learning or transfer learning with existing hyperspectral libraries, could also improve anomaly detection confidence and reduce the need for optimal threshold selection.

## VI. CONCLUSION

This research introduced the Exponentially moving RX (ERX) algorithm for real-time anomaly detection in hyperspectral line-scanning. ERX is fast and scalable to the high dimensions of hyperspectral imagery. It adapts quickly to



changing scenery and is robust in detecting anomalies using less corrected data (radiance instead of reflectance).

Tuning ERX's momentum parameter (exponential decay) improves detection performance based on the anomaly frequency and the variation of the scenery. Three datasets were introduced, and four other algorithms were implemented on-board a Jetson Xavier NX compute module to evaluate ERX's performance. ERX excelled in detection and speed on the beach dataset, being the only algorithm fast enough to run in real-time. ERX had the best detection performance on the synthetic dataset, and it was the fastest algorithm on the SNP dataset.

Overall, ERX had the strongest combined performance, but the datasets were challenging for all algorithms. This highlights the need for new anomaly detection methods. There are promising pathways for future work in anomaly detection for hyperspectral line-scanning in real-time (or near real-time); particularly with unsupervised and self-supervised algorithms that group anomalous pixels into objects and locate them, adaptive or automatic threshold selection, and field tests that validate the algorithms' practicality.

#### ACKNOWLEDGMENT

The authors thank Dr. Yiwei Mao for his comments on the paper and advice regarding the beach dataset, and Mr. Anthony Quach and Dr. Robert Winter for their general support.

#### REFERENCES

- [1] C.-I. Chang and S.-S. Chiang, "Anomaly detection and classification for hyperspectral imagery," *IEEE transactions on geoscience and remote sensing*, vol. 40, no. 6, pp. 1314–1325, 2002.
- [2] C. Corradino, E. Amato, F. Torrisi, and C. Del Negro, "Data-driven random forest models for detecting volcanic hot spots in sentinel-2 msi images," *Remote Sensing*, vol. 14, no. 17, p. 4370, 2022.
- [3] P. Bergmann, M. Fauser, D. Sattlegger, and C. Steger, "Mvtec ad—a comprehensive real-world dataset for unsupervised anomaly detection," in *Proceedings of the IEEE/CVF conference on computer vision and pattern recognition*, 2019, pp. 9592–9600.
- [4] T. Schlegl, P. Seeböck, S. M. Waldstein, U. Schmidt-Erfurth, and G. Langs, "Unsupervised anomaly detection with generative adversarial networks to guide marker discovery," in *International conference on information processing in medical imaging*. Springer, 2017, pp. 146–157.
- [5] G. P. Asner, R. E. Martin, D. Knapp, R. Tupayachi, C. Anderson, F. Sinca, N. Vaughn, and W. Lactayo, "Airborne laser-guided imaging spectroscopy to map forest trait diversity and guide conservation," *Science*, vol. 355, no. 6323, pp. 385–389, 2017.
- [6] N. Farmonov, K. Amankulova, J. Szatmári, A. Sharifi, D. Abbasi-Moghadam, S. M. M. Nejad, and L. Mucsi, "Crop type classification by desis hyperspectral imagery and machine learning algorithms," *IEEE Journal of selected topics in applied earth observations and remote sensing*, vol. 16, pp. 1576–1588, 2023.
- [7] Z. Pei, G. Han, H. Mao, C. Chen, T. Shi, K. Yang, X. Ma, and W. Gong, "Improving quantification of methane point source emissions from imaging spectroscopy," *Remote Sensing of Environment*, vol. 295, p. 113652, 2023.
- [8] L. Papp, B. Van Leeuwen, P. Szilassi, Z. Tobak, J. Szatmári, M. Árvai, J. Mészáros, and L. Pásztor, "Monitoring invasive plant species using hyperspectral remote sensing data," *Land*, vol. 10, no. 1, p. 29, 2021.
- [9] R. O. Green, N. Mahowald, C. Ung, D. R. Thompson, L. Bator, M. Bennet, M. Bernas, N. Blackway, C. Bradley, J. Cha *et al.*, "The earth surface mineral dust source investigation: An earth science imaging spectroscopy mission," in *2020 IEEE aerospace conference*. IEEE, 2020, pp. 1–15.
- [10] M. K. Lehmann, D. Gurlin, N. Pahlevan, K. Alikas, T. Conroy, J. Anstee, S. V. Balasubramanian, C. C. Barbosa, C. Binding, A. Bracher *et al.*, "Gloria-a globally representative hyperspectral in situ dataset for optical sensing of water quality," *Scientific data*, vol. 10, no. 1, p. 100, 2023.
- [11] S. Matteoli, M. Diani, and G. Corsini, "A tutorial overview of anomaly detection in hyperspectral images," *IEEE Aerospace and Electronic Systems Magazine*, vol. 25, no. 7, pp. 5–28, 2010.
- [12] M. T. Eismann, A. D. Stocker, and N. M. Nasrabadi, "Automated hyperspectral cueing for civilian search and rescue," *Proceedings of the IEEE*, vol. 97, no. 6, pp. 1031–1055, 2009.
- [13] C. M. Stellman, G. G. Hazel, F. Bucholtz, J. V. Michalowicz, A. D. Stocker, and W. Schaaf, "Real-time hyperspectral detection and cuing," *Optical Engineering*, vol. 39, no. 7, pp. 1928–1935, 2000.
- [14] P. Horstrand, M. Díaz, R. Guerra, S. López, and J. F. López, "A novel hyperspectral anomaly detection algorithm for real-time applications with push-broom sensors," *IEEE Journal of Selected Topics in Applied Earth Observations and Remote Sensing*, vol. 12, no. 12, pp. 4787–4797, 2019.
- [15] J. P. Kerekes and J. R. Schott, "Hyperspectral imaging systems," *Hyperspectral data exploitation: Theory and applications*, pp. 19–45, 2007.
- [16] H. Aasen, E. Honkavaara, A. Lucieer, and P. J. Zarco-Tejada, "Quantitative remote sensing at ultra-high resolution with uav spectroscopy: a review of sensor technology, measurement procedures, and data correction workflows," *Remote Sensing*, vol. 10, no. 7, p. 1091, 2018.
- [17] I. S. Reed and X. Yu, "Adaptive multiple-band cfar detection of an optical pattern with unknown spectral distribution," *IEEE transactions on acoustics, speech, and signal processing*, vol. 38, no. 10, pp. 1760–1770, 1990.
- [18] H. Su, Z. Wu, H. Zhang, and Q. Du, "Hyperspectral anomaly detection: A survey," *IEEE Geoscience and Remote Sensing Magazine*, vol. 10, no. 1, pp. 64–90, 2021.
- [19] S.-Y. Chen, Y. Wang, C.-C. Wu, C. Liu, and C.-I. Chang, "Real-time causal processing of anomaly detection for hyperspectral imagery," *IEEE transactions on aerospace and electronic systems*, vol. 50, no. 2, pp. 1511–1534, 2014.
- [20] Q. Du and R. Nekovei, "Fast real-time onboard processing of hyperspectral imagery for detection and classification," *Journal of Real-Time Image Processing*, vol. 4, no. 3, pp. 273–286, 2009.
- [21] S. Liu, M. Song, B. Xue, C.-I. Chang, and M. Zhang, "Hyperspectral real-time local anomaly detection based on finite markov via line-by-line processing," *IEEE Transactions on Geoscience and Remote Sensing*, 2023.
- [22] L. Zhang, B. Peng, F. Zhang, L. Wang, H. Zhang, P. Zhang, and Q. Tong, "Fast real-time causal linewidth progressive hyperspectral anomaly detection via cholesky decomposition," *IEEE Journal of Selected Topics in Applied Earth Observations and Remote Sensing*, vol. 10, no. 10, pp. 4614–4629, 2017.
- [23] C. Zhao and Y. Xi-Feng, "Fast real-time kernel rx algorithm based on cholesky decomposition," *IEEE Geoscience and Remote Sensing Letters*, vol. 15, no. 11, pp. 1760–1764, 2018.
- [24] C. Zhao, X. Yao, and B. Huang, "Real-time anomaly detection based on a fast recursive kernel rx algorithm," *Remote Sensing*, vol. 8, no. 12, p. 1011, 2016.
- [25] C. Zhao, C. Li, X. Yao, and W. Li, "Real-time kernel collaborative representation-based anomaly detection for hyperspectral imagery," *Infrared Physics & Technology*, vol. 107, p. 103325, 2020.
- [26] W. Li and Q. Du, "Collaborative representation for hyperspectral anomaly detection," *IEEE Transactions on geoscience and remote sensing*, vol. 53, no. 3, pp. 1463–1474, 2014.
- [27] H. Kwon, S. Z. Der, and N. M. Nasrabadi, "Adaptive anomaly detection using subspace separation for hyperspectral imagery," *Optical Engineering*, vol. 42, no. 11, pp. 3342–3351, 2003.
- [28] A. Rossi, N. Acito, M. Diani, and G. Corsini, "Rx architectures for real-time anomaly detection in hyperspectral images," *Journal of real-time image processing*, vol. 9, no. 3, pp. 503–517, 2014.
- [29] N. Acito, S. Matteoli, M. Diani, and G. Corsini, "Complexity-aware algorithm architecture for real-time enhancement of local anomalies in hyperspectral images," *Journal of real-time image processing*, vol. 8, no. 1, pp. 53–68, 2013.
- [30] C. Zhao, Y. Wang, B. Qi, and J. Wang, "Global and local real-time anomaly detectors for hyperspectral remote sensing imagery," *Remote sensing*, vol. 7, no. 4, pp. 3966–3985, 2015.
- [31] H. Kwon and N. M. Nasrabadi, "Kernel rx-algorithm: A nonlinear anomaly detector for hyperspectral imagery," *IEEE transactions on Geoscience and Remote Sensing*, vol. 43, no. 2, pp. 388–397, 2005.
- [32] C. Zhao, W. Deng, Y. Yan, and X. Yao, "Progressive line processing of kernel rx anomaly detection algorithm for hyperspectral imagery," *Sensors*, vol. 17, no. 8, p. 1815, 2017.
- [33] M. Díaz, R. Guerra, P. Horstrand, S. López, and R. Sarmiento, "A line-by-line fast anomaly detector for hyperspectral imagery," *IEEE*

- Transactions on Geoscience and Remote Sensing*, vol. 57, no. 11, pp. 8968–8982, 2019.
- [34] M. Díaz, R. Guerra, S. López, J. Caba, and J. Barba, “An fpga-based implementation of a hyperspectral anomaly detection algorithm for real-time applications,” in *2021 IEEE International Geoscience and Remote Sensing Symposium IGARSS*. IEEE, 2021, pp. 1579–1582.
  - [35] J. Caba, M. Díaz, J. Barba, R. Guerra, S. Escolar, and S. López, “Low-power hyperspectral anomaly detector implementation in cost-optimized fpga devices,” *IEEE Journal of Selected Topics in Applied Earth Observations and Remote Sensing*, vol. 15, pp. 2379–2393, 2022.
  - [36] Y. Mao, C. H. Betters, B. Evans, C. P. Artlett, S. G. Leon-Saval, S. Garske, I. H. Cairns, T. Cocks, R. Winter, and T. Dell, “Openhsi: A complete open-source hyperspectral imaging solution for everyone,” *Remote Sensing*, vol. 14, no. 9, p. 2244, 2022.
  - [37] R. O. Green, M. L. Eastwood, C. M. Sarture, T. G. Chrien, M. Aronsson, B. J. Chippendale, J. A. Faust, B. E. Pavri, C. J. Chovit, M. Solis *et al.*, “Imaging spectroscopy and the airborne visible/infrared imaging spectrometer (aviris),” *Remote sensing of environment*, vol. 65, no. 3, pp. 227–248, 1998.
  - [38] P. Ghomb and M. Romaszewski, “Anomaly detection in hyperspectral remote sensing images,” in *Hyperspectral Remote Sensing*. Elsevier, 2020, pp. 45–66.
  - [39] S. K. Lam, A. Pitrou, and S. Seibert, “Numba: A llvm-based python jit compiler,” in *Proceedings of the Second Workshop on the LLVM Compiler Infrastructure in HPC*, 2015, pp. 1–6.
  - [40] Q. Wang, X. Zhang, Y. Zhang, and Q. Yi, “Augem: automatically generate high performance dense linear algebra kernels on x86 cpus,” in *Proceedings of the international conference on high performance computing, networking, storage and analysis*, 2013, pp. 1–12.
  - [41] J. Redmon, S. Divvala, R. Girshick, and A. Farhadi, “You only look once: Unified, real-time object detection,” in *Proceedings of the IEEE conference on computer vision and pattern recognition*, 2016, pp. 779–788.
  - [42] J.-T. Lin and C.-H. Lin, “Real-time hyperspectral anomaly detection using collaborative superpixel representation with boundary refinement,” in *IGARSS 2022-2022 IEEE International Geoscience and Remote Sensing Symposium*. IEEE, 2022, pp. 1752–1755.